

2 In situ calibration of the single photoelectron charge 3 response of the IceCube photomultipliers

IceCube author list to be inserted... E-mail: `analyses@icecube.wisc.edu`

ABSTRACT: This article outlines the in situ calibration of the single photoelectron charge distributions for each of the Hamamatsu Photonics R7081-02 photomultipliers in the IceCube Neutrino Observatory. The accurate characterization of the individual PMT charge distributions is important for event reconstruction and calibration. We discuss the single photoelectron identification procedure and how we extract the single photoelectron charge distribution using a deconvolution of the multiphotoelectron charge distribution, and we examine various correlations between the shape of the single photoelectron charge distribution and various hardware components. The time dependence of the charge distributions is also investigated.

Definitions (this will be removed in the final draft):

1. Charge: WaveDeform fits the waveform with an SPE pulses template. The integral of the fitted pulse, divided by the load resistance, divided by the gain, is the reported measured *charge* of the pulse. It is reported in units of a single electron.
2. PE: The unit of charge. This represents the charge relative to one electron.
- 4 3. 1 PE: The HV on each DOM is set such that the gain on the PMT is 10^7 . It is determined to be at the proper gain (10^7), when the Gaussian mean of the fitted charge distribution is at 1 PE.
4. Photoelectron: The physical electron emitted from the photocathode.
5. SPE: (Single Photoelectron) A single physical electron emitted from the photocathode.
6. MPE: (Multiple Photoelectron): multiple electrons emitted from the photocathode, charges may have been combined.
7. Charge distribution: The distribution of the measured charges. This will include both SPE and MPE events.
8. Single Photoelectron Charge distribution: The hypothetical charge distribution generated by observing a pure sample of single photoelectron.
9. SPE Template: The functional form that is used to fit the charge distribution.

5 KEYWORDS: IceCube, single photoelectron, charge distribution, PMT.

7 Contents

8	1. Introduction	1
9	1.1 Single photoelectron charge distributions	3
10	1.2 IceCube datasets and software definitions	5
11	2. Extracting the SPE templates	6
12	2.1 Single photoelectron pulse selection	6
13	2.2 Characterizing the low-charge region	8
14	2.3 Fitting procedure	8
15	2.4 SPE template fit results	9
16	3. Discussion	10
17	3.1 Correlations between fit parameters and DOM hardware differences	10
18	3.2 Quantifying observable changes when modifying the PMT charge distributions	13
19	3.2.1 Model comparison	14
20	3.3 SPE templates in simulation	14
21	3.4 SPE templates for calibration	15
22	4. Conclusion	16

24 1. Introduction

25 The IceCube Neutrino Observatory [1, 2] is a cubic-kilometer-sized array of 5,160 photomultiplier
 26 tubes (PMTs) buried in the Antarctic ice sheet designed to observe high-energy neutrinos interact-
 27 ing with the ice [3]. In 2011, the IceCube Collaboration completed the installation of 86 vertical
 28 *strings* of PMT modules, eight of which were arranged in a denser array for the DeepCore detec-
 29 tor [4] and the remaining for the main IceCube detector. Each string in the detector contains 60
 30 digital optical modules (DOMs), that contain a single PMT each, as well as all required electron-
 31 ics [5]. The DOMs extend from 1450 m to 2450 m below the surface of the ice sheet and are spaced
 32 17 m apart in the IceCube detector, and 7 m apart in the DeepCore detector.

33 Each DOM consists of a 0.5" thick spherical glass pressure vessel that houses a single down
 34 facing 10" R7081-02 PMT from Hamamatsu Photonics [6]. The PMT is specified for wavelengths
 35 ranging from 300 nm to 650 nm, with peak quantum efficiency of 25% near 390 nm, classified as
 36 normal quantum efficiency (NQE) DOMs. Each PMT is coupled to the glass housing with optical
 37 gel and is surrounded by a wire mesh of μ metal to reduce the effect of the Earth's ambient magnetic
 38 field. Then glass housing is transparent to wavelengths 350 nm and above [7].

39 IceCube has also deployed 399 DOMs with Hamamatsu R7081-02MOD PMTs, which, having
 40 a peak quantum efficiency of 34% near 390 nm (36% higher efficiency than the standard DOMs),

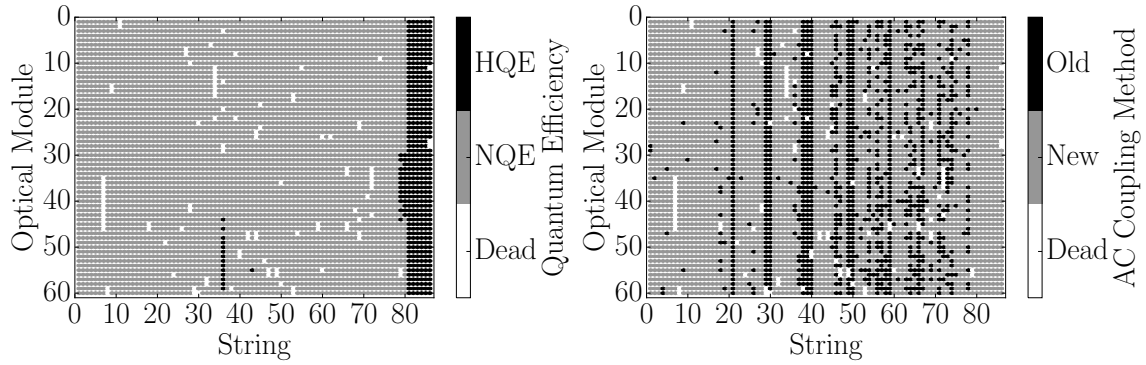


Figure 1. Left: A mapping of the HQE DOMs (black) and standard NQE DOMs (gray). Right: The version of AC coupling, old toroids (black) and new toroids (gray). DOMs that have been removed from service are shown in white.

41 are classified as high quantum efficiency (HQE) DOMs [4]. These DOMs are primarily located in
 42 DeepCore and on strings 36 and 43, as shown in the left side of Fig. 1.

43 The R7081-02 and R7081-02MOD PMTs have 10 dynode stages and are operated with a gain
 44 of 10^7 and high voltage around 1200 V (a typical amplified single photoelectron will generate a
 45 ≈ 6 mV peak voltage at the input to the front-end amplifiers). The PMTs operate with the anodes
 46 at high voltage and the signal is AC coupled to the front-end amplifiers. There are two versions
 47 of AC coupling in the detectors, both of which use custom-designed wideband bifilar wound 1:1
 48 toroidal transformers¹ (the DOM-specific AC-coupling versions, new and old toroids, are shown
 49 on the right side of Fig. 1). The DOMs with the old toroids were designed with an impedance of
 50 43Ω , while the new toroids are 50Ω [8].

51 IceCube relies on two observables per DOM to reconstruct events: the total number of detected
 52 photons and their timing distribution. Both the timing and the number of photons are extracted from
 53 the on-board digitized waveforms in software. The waveforms are deconvolved into a series of
 54 scaled single-photoelectron pulses (so-called pulse series) and the integral of the individual pulses
 55 (divided by the load resistance) defines the observed charge. It will often be expressed in units of
 56 PE, or photoelectrons, which further divides the measured charge by the charge of a single electron
 57 times the nominal gain (10^7). Accurate characterization of the individual PMT charge distributions
 58 is crucial for calibration and event reconstructions relying on charge information. The charge
 59 distribution can also be used to assess long term detector performance and identifying discrepancies
 60 between data and Monte Carlo. It is therefore critically important to accurately measure the single
 61 photoelectron charge distribution in order to understand the IceCube detector behavior.

62 When one or more photons produce a voltage at the anode sufficient to trigger the onboard
 63 discriminator (set via a DAC to approximately 1.3 mV, or equivalently to 0.25PE), the signal ac-
 64 quisition process is triggered. The signal is fed into four parallel input channels. Three of the

¹Conventional AC-coupling high-voltage ceramic capacitors can produce noise from leakage currents and impractical requirements on the capacitors in order to meet the signal droop and undershoot requirements. The toroidal transformer effectively acts as a high-pass filter with good signal fidelity at high frequencies. It also provides higher reliability than capacitive coupling and reduces the stored energy, which might cause damage if there is HV discharge in the system [7]. However, the toroidal-transformer AC coupling also introduces signal droop and undershoot.

65 channels pass first through a 75 ns delay loop in order to capture the leading edge of the pulse
66 and then into three high-speed (300 MSPS for 128 samples) 10-bit waveform digitizers (Analog
67 Transient Waveform Digitizer, ATWD), each of which has a different level of amplification (15.7
68 ± 0.6 , 1.79 ± 0.06 , and 0.21 ± 0.01 [8]). There are also three extra ATWDs on board each DOM:
69 one is used for calibration and the other two operate in a ping-pong fashion to remove dead time
70 associated with the readout. The signal to the fourth channel is first shaped and amplified and then
71 fed into a 10-bit fast analog-to-digital converter (fADC) operating at a sampling speed of 40 MSPS.
72 Further detail regarding the description of the DOM electronics can be found in Refs. [5, 9].

73 This article discusses the accurate determination of how individual DOMs collect charge in
74 order to improve calibration and the detector description as used in the IceCube Monte Carlo sim-
75 ulation. It describes the procedure for determining the PMT’s gain characteristics as seen in the
76 single-photoelectron (SPE) charge distributions using in situ data from the IceCube and DeepCore
77 detectors. The SPE charge distribution refers to the measured charge probability density function
78 of the individual DOMs generated by the amplification of a pure sample of single photoelectrons.
79 The extraction of the SPE charge distribution was recently made possible from the development of
80 two pieces of software:

- 81 1. A specially designed unbiased pulse selection was developed to reduce the MPE contamina-
82 tion while accounting for physical phenomena (e.g., late pulses, afterpulses, pre-pulses, and
83 baseline shifts) and software-related effects (e.g., pulse splitting). This is further described
84 in Sec. 2.1.
- 85 2. A fitting procedure was developed that separates the remaining MPE contamination from the
86 SPE charge distribution by deconvolving the measured charged distribution. This is further
87 described in Sec. 2.3.

88 By using in situ data to determine the SPE charge distributions, we accurately represent the
89 individual PMT response as a function of time, environmental conditions, software version, and
90 hardware differences, and we sample photons uniformly over the surface of the photocathode. This
91 is beneficial since it also allows us to inspect the stability and long-term behavior of the individual
92 DOMs, verify previous calibration, and correlate features and environment to DOM behavior.

93 **1.1 Single photoelectron charge distributions**

94 In an idealized scenario, a single photon produces a single photoelectron, which is then amplified by
95 a known amount and the measured charge corresponds to 1 PE. However, there are many physical
96 processes that create structure in the measured charge distributions. For example:

- 97 • **Statistical fluctuation due to cascade multiplication** [10]. At every stage of dynode am-
98 plification, there is a stochastic spread in the number of emitted electrons that make it to the
99 next dynode. This in turn causes a spread in the measured charge after the gain stage of the
100 PMT.
- 101 • **Photoelectron trajectory**. Some electrons may deviate from the favorable trajectory, reduc-
102 ing the number of secondaries produced at a dynode or the efficiency to collect them on the

103 following dynode. This can occur at any stage, but it has the largest effect on the multipli-
104 cation at the first dynode [11]. The trajectory of a photoelectron striking the first dynode
105 will depend on many things, include where on the photocathode it was emitted, the unifor-
106 mity of the electric field, the size and shape of the dynodes [10], and the ambient magnetic
107 field [12, 13].

108 • **Late or delayed pulses.** A photoelectron can elastically or inelastically scatter off the first
109 dynode. The scattered electron can then be re-accelerated to the dynode, creating a second
110 pulse. The difference in time between the initial pulse and the re-accelerated pulse in the
111 R7081-02 PMT was previously measured to be up to 70 ns [7, 14]. The two subpulses have
112 lower charges, but the sum of the two tends to add up to the original charge. Collecting either
113 the initial pulse or the late pulse will result in the charge being reconstructed in the low-PE
114 region [15].

115 • **Afterpulses.** When a photoelectron or the secondary electrons produced during the electron
116 cascade gain sufficient energy to ionize residual gas in the PMT, the positively charged ion-
117 ized gas will be accelerated in the electric field towards the photocathode. Upon impact with
118 the photocathode, electrons can be again released from the photocathode, creating what is
119 called an afterpulse. For the R7081-02 PMTs, the timescale for afterpulses was measured
120 to occur from 0.3 to 11 μ s after the initial pulse, with the first prominent afterpulse peak
121 occurring at approximately 600 ns [7]. The spread in the afterpulse time is dependent on
122 the position of photocathode, the charge-to-mass ratio of the ion produced, and the electric
123 potential distribution [16], whereas the size of the afterpulse is related to the momentum and
124 species of the ionized gas and composition of the photocathode [17].

125 • **Pre-pulses.** If an incident photon passes through the photocathode without interaction and
126 strikes one of the dynodes, it can eject an electron that is only amplified by the subsequent
127 stages, resulting in a lower measured charge (lower by a factor of approximately 25). For
128 the IceCube PMTs, the prepulses were found to arrive approximately 30 ns before the signal
129 from other photoelectrons from the photocathode [7].

130 • **MultiPE contamination.** When multiple photoelectrons arrive at the first dynodes within
131 several nanoseconds of each other, they can be reconstructed by the software as a single,
132 multiPE pulse.

133 • **Electronic noise.** This refers to the fluctuations in the analog-to-digital converters (ATWDs
134 and FADC) and ringing that arises from the electronics.

135 Beyond the physical phenomena above that modify the measured charge distribution, there is
136 also a lower limit on the smallest charge that can be extracted. For IceCube, the discriminator limits
137 the trigger pulse to be above approximately 0.25PE, and subsequent pulses in the readout time
138 window are subject to a software-defined threshold. The software threshold was set conservatively
139 to avoid extracting pulses that originated from electronic noise. This threshold can be modified to
140 gain access to lower charge pulses and will be discussed in Sec. 2.2.

141 The standard charge distribution model used by the IceCube Collaboration (known as the
 142 TA0003 distribution [7]) represented the above effects as the sum of an exponential plus a Gaussian,
 143 where the exponential represented charge of poorly amplified pulses and the Gaussian represented
 144 the spread in statistical fluctuations due to the cascade multiplication. The TA0003 distribution was
 145 previously used to describe all the PMTs in the IceCube and DeepCore detectors.

146 Recently, IceCube has performed several lab measurements using the R7081-02 PMTs with in-
 147 time laser pulses, demonstrating that the in-time charge distribution includes a steeply falling low-
 148 charge component below the discriminator threshold. To account for this, a new functional form
 149 including a second exponential was introduced. This form of the charge distribution, $f(q)_{SPE} =$
 150 $Exp_1 + Exp_2 + \text{Gaussian}$, is referred to as the *SPE template* in this report. Explicitly, it is:

$$f(q)_{SPE} = E_1 e^{-q/w_1} + E_2 e^{-q/w_2} + N e^{-\frac{(q-\mu)^2}{2\sigma^2}}, \quad (1.1)$$

151 where q represents the measured charge; E_1 , E_2 , and N represent normalization factors of each
 152 components; w_1 and w_2 are the exponential decay widths; and μ , σ are the Gaussian mean and
 153 width, respectively. This is the assumed functional shape of the SPE charge distributions and the
 154 components of Eq. 1.1 are determined in this report for all in-ice DOMs. IceCube defines 1 PE as
 155 the location of the Gaussian mean (μ) and calibrates the gain on the individual PMTs during the
 156 start of each season to meet this definition. This definition comes from the Gaussian fit component
 157 aimed at modeling the statistical fluctuations of the cascade multiplication process assuming the
 158 central limit theorem (see Sec. 1.1).

159 1.2 IceCube datasets and software definitions

160 The largest contribution to the IceCube trigger rate comes from downgoing muons produced in
 161 cosmic ray induced showers [18]. Cosmic ray muons stopping in the detector cause the individual
 162 trigger rate to decrease at lower depths. Further, during the formation of this ice sheet, there have
 163 been several periods of colder climate that have caused the optical properties of the ice to differ
 164 at various depths. The optical properties also affect the trigger rate; in particular, the “dust layer”
 165 from 2100 to 2200 m below the surface (optical modules 32 to 38 in the IceCube detector) is a
 166 region in the ice with a relatively large scattering and absorption coefficient [19].

167 An induced signal in the PMT that passes through the AC coupling toroid located on the base
 168 of the PMT is compared to a discriminator threshold. If two DOMs within two DOM distances of
 169 each other observe a passing of the discriminator, a *hard local coincidence* (HLC) is initiated and
 170 the corresponding waveforms are sampled 128 times and read out on the three ATWDs.

171 After waveform digitization, there is a correction applied to remove the measured DC baseline
 172 offset. The signal droop and undershoot introduced by the toroidal transformer AC coupling is
 173 compensated for in software (during waveform calibration) by adding the expected temperature-
 174 dependent reaction voltage of the undershoot to the calibrated waveform. Conditions where the
 175 undershoot voltage drops below 0 ADC counts, the ADC values are zeroed and then compensated
 176 for once the waveform is above the minimum ADC input. Scaled single photoelectron pulse shapes
 177 (that take into account the version of the AC coupling) are then fit to the waveforms using software
 178 referred to as WaveDeform (waveform unfolding process), which determines the individual pulse
 179 time stamp and charge and populates a pulse series [20].

180 The pulse series used in this analysis come from two datasets provided by IceCube:

- 181 1. The **MinBias dataset**. This dataset records the full waveform readout of randomly triggered
182 HLC events at a rate that corresponds on average to 1/1000 events. The largest contribution
183 to the IceCube trigger rate comes from downgoing muons produced in cosmic ray induced
184 showers [18] and therefore is the largest signal component in this dataset. These muons tend
185 to have small energies when they reach the detector, thus they produce minimal MPE con-
186 tamination. The full waveform of these events allows us to extract the raw information about
187 the individual pulses. This will be used to measure the individual PMT charge distributions.

- 188 2. The **BeaconLaunch dataset**. This is a forced trigger (not triggered by the discriminator)
189 filter that is typically used to monitor the individual DOM baseline. It includes the full
190 ATWD window waveform readout. Since this dataset is forced triggered, the majority of
191 these waveforms represent baseline fluctuations with minimal contamination from the occa-
192 sional coincidental pulse that makes it into the readout window. This dataset will be used to
193 examine the noise contribution to the charge distributions. Note: when using this dataset, the
194 weight of every pulse is multiplied by a factor of 28.4 to account for the livetime difference
195 between the MinBias dataset and the BeaconLaunch dataset. Weight, in this context, refers to
196 the number of photons in the MinBias dataset equivalent to one photon in the BeaconLaunch
197 dataset for which both datasets have the same equivalent livetime.

198 This analysis uses the full MinBias and BeaconLaunch datasets from IceCube seasons 2011
199 to 2016 (subsequently referred to as IC86.2011 to IC86.2016). Seasons in IceCube typically start
200 in June of the labeled year and end approximately one year later. Calibration is performed at the
201 beginning of each season.

202 2. Extracting the SPE templates

203 2.1 Single photoelectron pulse selection

204 The pulse selection is the method used to extract candidate, unbiased, single photoelectron pulses
205 from data while minimizing the multiPE contamination. It avoids collecting afterpulses, rejects late
206 pulses from the trigger, reassembles late pulses, accounts for the discriminator threshold, reduces
207 the effect of droop and baseline undershoot, and gives sufficient statistics to perform a season-to-
208 season measurement. An illustrative diagram of the pulse selection is shown in the left side of
209 Fig. 2, while a description of the procedure is detailed below.

210 In order to trigger a DOM, the input to the front-end amplifiers must exceed the discriminator
211 threshold. To avoid the selection bias of the discriminator trigger, we ignore the trigger pulse as
212 well as the entire first 100 ns of the time window. Ignoring the first 100 ns has the added benefit
213 of also removing late pulses that could be attributed to the triggering pulse. To ensure we are not
214 accepting afterpulses into the selection, we also enforce the constraint that the pulse of interest
215 (POI) is within the first 375 ns of the ATWD time window. This also allows us to examine the
216 waveform up to 50 ns after the POI (the ATWD time window is ≈ 425 ns). In the vicinity of the
217 POI, we check that WaveDeform did not reconstruct any pulses up to 50 ns prior to the POI, or 100

218 to 150 ns after the POI (the light gray region of Fig. 2 (left)). This later constraint is to reduce the
 219 probability of accidentally splitting a late pulse in the summation window.

220 Restrictions are put on the full ATWD waveforms as well, so as to ensure that the trigger pulse
 221 does not exceed 10 mV (to reduce the effect of the subsequent baseline undershoot due to the AC
 222 coupling or other artifacts from large pulses), and a global constraint ensures that the time window
 223 cannot contain any waveform that exceeds 20 mV (recall that a properly amplified SPE pulse is
 224 ≈ 6 mV).

225 If a pulse is reconstructed between 100 and 375 ns after the time window is opened and the
 226 voltage criteria are met, it is accepted as a candidate photoelectron and several checks are performed
 227 on the waveform prior to and after the pulse. The first check is to ensure that the waveform is near
 228 the baseline just before the rising edge of the POI. This is accomplished by ensuring that the
 229 waveform does not exceed 1 mV, 50 to 20 ns prior to the POI, and eliminates cases where the POI
 230 is a late pulse. We also ensure the waveform returns to the baseline by checking that no ADC
 231 measurement exceeds 1 mV, 100 to 150 ns after the POI (these constraints are illustrated as the
 232 horizontal red dotted lines and black arrows in the left side of Fig. 2).

233 If all the above criteria are met, we sum the reconstructed charges from the POI time (given
 234 by WaveDeform) to +100 ns (the dark gray area in Fig. 2 (left)). This ensures that any nearby
 235 pulses are either fully separated or fully added. WaveDeform may occasionally split an SPE pulse
 236 into multiple smaller pulses, therefore it is always critical to perform a summation of the charge
 237 within a window. The 100 ns summation also means that the pulse selection will occasionally be
 238 accepting MPE events.

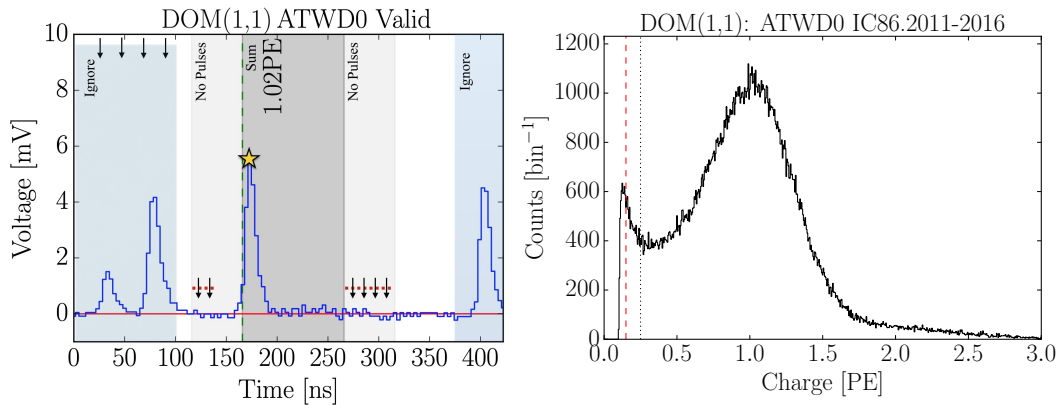


Figure 2. Left: An illustrative diagram of the pulse selection criteria for selecting a high-purity and unbiased sample of single photoelectrons. The digitized ATWD waveform is shown in blue. The pulse of interest is identified with a yellow star. This example waveform was triggered by a small pulse at 25 ns (recall that the delay board allows us to examine the waveform just prior to the trigger pulse), followed by a potential late pulse at 70 ns. At 400 ns, we see a pulse in the region susceptible to afterpulses. Waveform voltage checks are illustrated with arrows, and various time windows described in the text are drawn with semiopaque regions. The POI is reported to have a charge of 1.02 PE, given by WaveDeform, and would pass the pulse selection criteria. Right: The collected charges from string 1, optical module 1 (DOM 1,1), from the MinBias dataset collected from IC86.2011 to IC86.2016 that pass the pulse selection. The discriminator threshold at 0.25PE is represented as a dotted black vertical line. For visual purposes, a vertical dashed red line is also included at 0.15PE.

239 **2.2 Characterizing the low-charge region**

240 Fig. 2 (right) shows the charge distributions of the selected pulses that pass the single photoelec-
 241 tron pulse selection for string 1, optical module 1 (DOM (1,1)). In the low-charge region (below
 242 0.25PE), we see a steep rise (in agreement with the in-time laser tests mentioned in Sec. 1.1), then
 243 a second threshold at approximately 0.13 PE. This is a software defined threshold that comes from
 244 a gradient-related termination condition in WaveDeform. The threshold was set to avoid electronic
 245 noise being interpreted as PMT pulses and contaminating the low-charge region. This section will
 246 examine the effect on the charge distribution and noise contribution by lowering the WaveDeform
 247 threshold. The aim will be to explore the low-charge region.

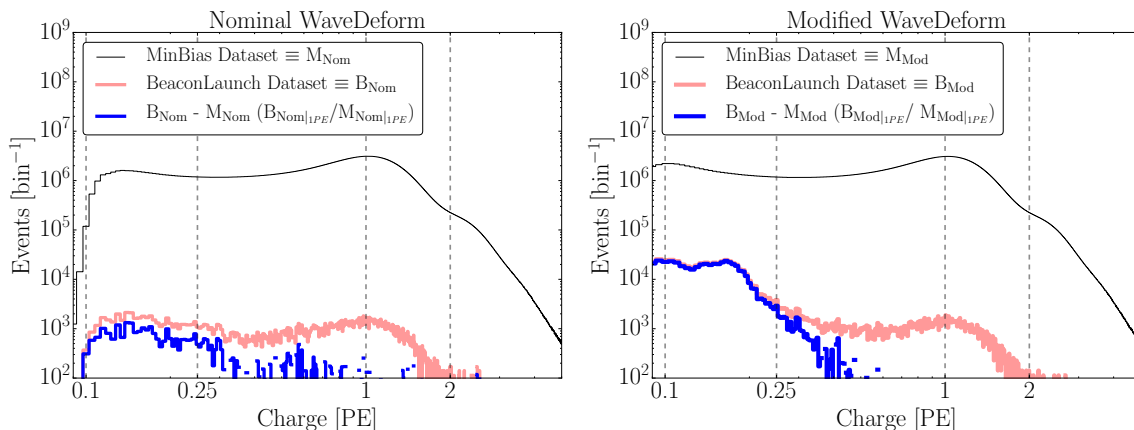


Figure 3. The cumulative charge distributions (IC86.2011 to 2016) of all DOMs for the MinBias and BeaconLaunch datasets. The blue histogram shows the expected contribution from noise (found by subtracting the shape of the MinBias dataset from the BeaconLaunch dataset). Left: The charge distributions for the standard WaveDeform settings. Right: The charge distributions for the modified WaveDeform settings.

248 Fig. 3 (left) shows the charge distributions for the MinBias (black) and the BeaconLaunch
 249 (red) datasets (left) using the default settings on WaveDeform. As mentioned in Sec. 1.2, occasionally
 250 a photoelectron will be coincident with the forced BeaconLaunch time window and populate a
 251 single photoelectron distribution. Subtracting the shape of the MinBias charge distribution from the
 252 BeaconLaunch dataset yields an estimate of the amount of electronic noise contamination (blue).
 253 The bin with the largest signal-to-noise ratio (SNR) above 0.1 PE was found to have 0.0013. The
 254 SNR for the full distribution was found to be 0.0005. Fig. 3 (right) shows the same data after
 255 lowering the WaveDeform threshold. Correspondingly, the bin with the largest SNR was found to
 256 be 0.0017, whereas the total SNR was found to be 0.0015.

257 **2.3 Fitting procedure**

258 The fit assumes that there is a negligible three-PE contribution, which is justified by the lack of
 259 statistics in the 3 PE region as well as the significant rate difference between the 1 PE and 2 PE
 260 region, as shown in Fig. 2 (right). The 2 PE charge distribution is assumed to be the SPE charge
 261 distribution convolved with itself [21]. A python-based piece of software called the "convolutional

262 fitter" is used to determine the components of Eq. 1.1 from the measured charge distribution that
 263 includes the multiPE contamination.

264 The Exp_2 component (as well as the Exp_1) of Eq. 1.1, represents poorly amplified photoelec-
 265 trons, and we do not allow it to extend beyond the high-charge region of the Gaussian component.
 266 In particular, we include a constraint on the the parameter w_2 to ensure that it falls off with the
 267 Gaussian component:

$$w_2 < \frac{\mu + 2\sigma}{4 - \text{Ln}(N/E_2)}. \quad (2.1)$$

268 This equation was found by setting the Exp_2 to be $1/e^2$ that of the Gaussian component at two
 269 sigma (the Exp_1 is neglected from this equation since it falls off in the low-charge region). Eq. 2.1
 270 is used as a constraint during the fit to the charge distributions.

271 Pulses that fall below the WaveDeform threshold and are not reconstructed contribute to an
 272 effective efficiency of the individual DOMs. This analysis assumes the same shape of the steeply
 273 falling exponential component (Exp_1) for all DOMs in the detector to avoid large fluctuations in
 274 the individual DOM efficiencies. The modified WaveDeform data will strictly be used to determine
 275 the Exp_1 component. Specifically, using the modified WaveDeform, we will background subtract
 276 the BeaconLaunch distribution from the MinBias data, fit the resulting distribution to determine
 277 the components of Eq. 2.1, and use only the measured shape and normalization of Exp_1 in all
 278 subsequent nonmodified WaveDeform fits.

279 Upon fitting the MinBias data (with the predetermine values for Exp_1), the residual of each
 280 fit is calculated by measuring the percentage difference between the fit and the data. The aver-
 281 age residual will then be used as a global scaling factor for all SPE templates to account for the
 282 difference between the chosen model (Eq. 2.1) and the actual data.

283 Failed fits (DOMs removed from service (109 DOMs) and DOMs that fail any one of several
 284 validity checks on the goodness of fit (6 DOMs)) are not included in this report. In the IceCube
 285 MC simulation chain, these DOMs are assigned the average SPE template.

286 2.4 SPE template fit results

287 Using the background subtracted modified WaveDe-
 288 form dataset, the steeply falling exponential com-
 289 ponent was determined by fitting the distribution
 290 from 0.1 PE to 3.5 PE to be $E_1 = 6.9 \pm 1.5$ and
 291 $w_1 = 0.032 \pm 0.002$ PE. The shape of the steeply falling
 292 exponential is then used to describe the low-PE charge
 293 region for all subsequent fits.

294 Using the MinBias dataset with the value for
 295 Exp_1 described above, the SPE templates are extracted
 296 for every DOM, separately for each IceCube season
 297 (IC86.2011 to IC86.2016). An average fit was also
 298 performed in which all the data for a given DOM was
 299 summed together (labeled as "AVG"). The fit range for

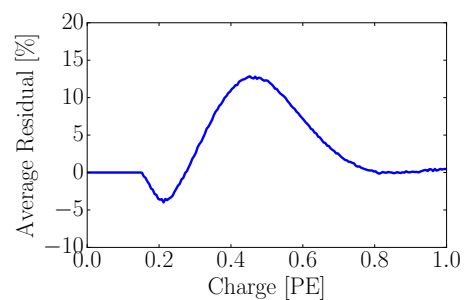


Figure 4. The measured average residual of the SPE templates fit.

300 Exp_2 and the Gaussian components are selected to be between 0.15 PE and 3.5 PE. The average
 301 residual for all DOMs from 0 to 1 PE is shown in Fig. 4.

302 An example fit is shown in Fig. 5 for the cumulative charge distribution for DOM (1,1). The
 303 collected charge distribution is shown in the black histogram, while the convolutional fit is shown
 304 as the black line (multiplied by the residual). The extracted SPE template (also multiplied by the
 305 residual) for this DOM is shown in blue.

306 The mean value and 1σ spread of the fit parameters, excluding Exp_1 , for the IceCube and
 307 DeepCore detectors are shown in Table 1 and Table 2, respectively.

308 The individual DOM SPE templates were then examined between IceCube seasons for a time
 309 dependence on the fit parameters. For every DOM, the change over time of each fit parameter
 310 (excluding Exp_1) was calculated.

311 Fig. 6 shows the change in a given fit parameter (represented as percentage deviation from the
 312 mean value), per year, of each DOM in both the IceCube (left) and DeepCore (right) detectors.
 313 The spread in the fit parameters was found to be consistent with statistically scrambling the yearly
 314 measurements. The average fit parameters are found to deviate less than 0.5% per year in both
 315 detectors, which is in agreement with the stability checks performed in Ref. [8].

316 3. Discussion

317 3.1 Correlations between fit parameters and DOM hardware differences

318 As noted in Sec. 1, there are two DOM-related hardware differences: the subset of HQE DOMs

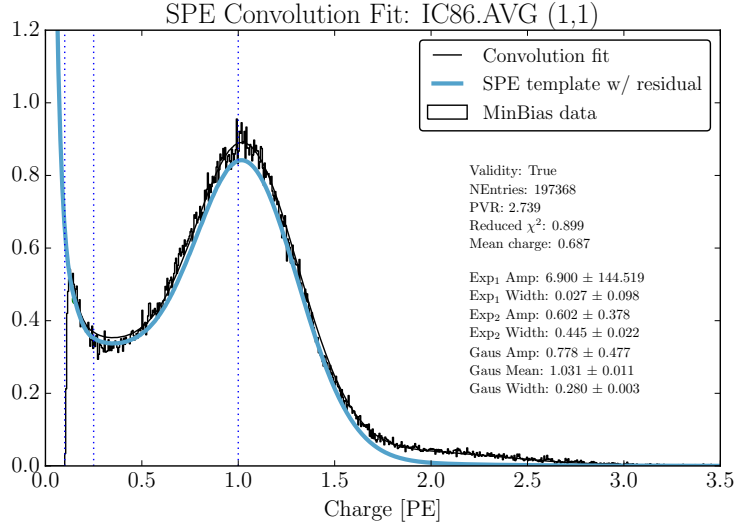


Figure 5. An example fit including the residual correction for DOM (1,1) using the WaveDeform dataset for seasons IC86.2011 to IC86.2016. The result from the convolutional fitter is shown as a solid black line. The extracted SPE template is shown blue. (SPENCER, remove the beacon launch from this image.) The purple histogram is the full-detector (all DOMs and all seasons summed together) BeaconLaunch dataset, multiplied to the livetime of the MinBias data and further multiplied by a factor of 100 in order to be visible on this plot.

IceCube	Exp ₂ Amplitude	Exp ₂ Width	Gaus. Amplitude	Gaus. Mean	Gaus. Width
IC86.2011	0.601 ± 0.101	0.457 ± 0.070	0.736 ± 0.061	1.022 ± 0.030	0.296 ± 0.033
IC86.2012	0.595 ± 0.100	0.462 ± 0.065	0.740 ± 0.062	1.020 ± 0.034	0.295 ± 0.033
IC86.2013	0.602 ± 0.101	0.452 ± 0.071	0.736 ± 0.060	1.021 ± 0.033	0.298 ± 0.032
IC86.2014	0.597 ± 0.099	0.453 ± 0.071	0.736 ± 0.059	1.019 ± 0.030	0.299 ± 0.030
IC86.2015	0.604 ± 0.099	0.457 ± 0.067	0.735 ± 0.061	1.024 ± 0.032	0.296 ± 0.032
IC86.2016	0.600 ± 0.101	0.460 ± 0.063	0.736 ± 0.060	1.024 ± 0.030	0.295 ± 0.031

Table 1. The average values and 1σ spread of each fit parameter for the IceCube detector. The active DOMs in the IceCube detector are 99.4% NQE, and 31.0% of these DOMs have the old method of AC coupling. Correspondingly, there are 0.6% HQE DOMs, and 69.0% of these DOMs have the new version of AC coupling.

DeepCore	Exp ₂ Amplitude	Exp ₂ Width	Gaus. Amplitude	Gaus. Mean	Gaus. Width
IC86.2011	0.519 ± 0.095	0.462 ± 0.099	0.763 ± 0.073	1.023 ± 0.031	0.307 ± 0.038
IC86.2012	0.517 ± 0.095	0.467 ± 0.098	0.763 ± 0.074	1.024 ± 0.032	0.306 ± 0.038
IC86.2013	0.520 ± 0.092	0.461 ± 0.096	0.763 ± 0.073	1.024 ± 0.030	0.306 ± 0.037
IC86.2014	0.522 ± 0.093	0.459 ± 0.098	0.765 ± 0.073	1.021 ± 0.031	0.306 ± 0.038
IC86.2015	0.525 ± 0.095	0.458 ± 0.099	0.763 ± 0.072	1.023 ± 0.031	0.307 ± 0.038
IC86.2016	0.522 ± 0.095	0.464 ± 0.098	0.763 ± 0.074	1.024 ± 0.031	0.305 ± 0.038

Table 2. The average values and 1σ spread of each fit parameter for the DeepCore detector. The active DOMs in DeepCore are 12.4% NQE, and 0.2% of these DOMs have the old method of AC coupling. Correspondingly, the DeepCore detector contains 87.6% HQE DOMs, and 99.8% of these DOMs have the new version of AC coupling.

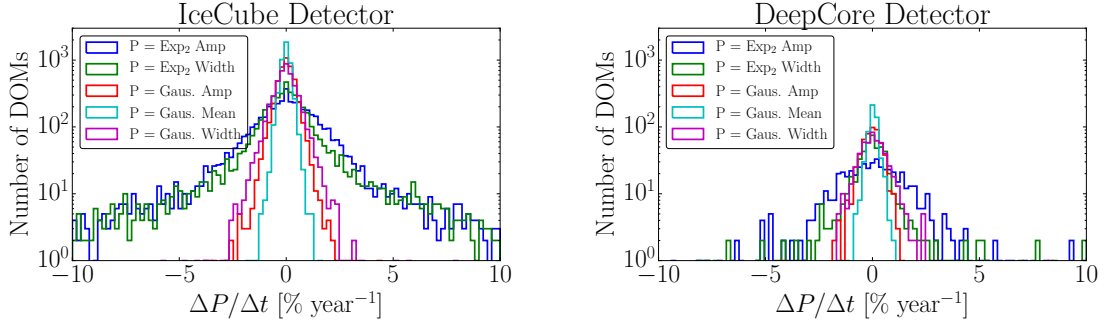


Figure 6. The change in individual DOM fitted parameters over time (Left: IceCube, Right: DeepCore). The change in the fit value is represented as percentage deviation from the mean fit parameter value.

319 and the version of AC coupling used to couple the signal from the PMT anode to the front-end am-
320 plifiers. Correlations between the different hardware configurations were examined for correlations
321 with the SPE template fit components.

322 The HQE DOMs were found to have a larger Exp₂ component (2.3% lower w_2 component, and
323 a 19.9% higher E_2 , described in terms of Eq.1.1) than the standard DOMs². Consequently, the HQE
324 DOMs have a 14.9% lower peak-to-valley ratio and a 3.3% lower mean charge. These distributions

²This difference is still observed when comparing the DOMs at similar depths in the detector.

325 are shown in Fig. 7. The change in the mean charge for the HQE DOMs is compensated for in
 326 simulation by increasing the HQE DOM efficiency by the equivalent amount. This ensures that the
 327 total amount of charge collected by the HQE DOMs remains the same after the SPE templates are
 328 implemented.

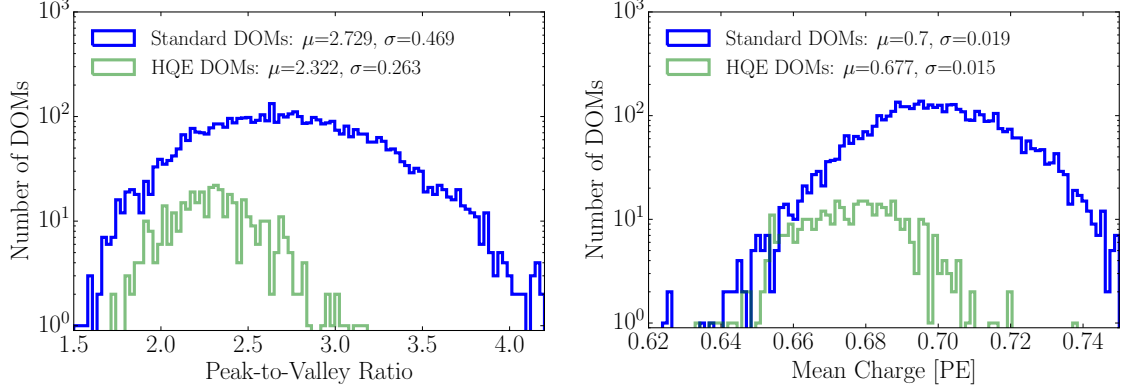


Figure 7. Comparison between the R7081-02MOD HQE DOMs and standard R7081-02 DOMs. Left: The peak-to-valley ratio for the two subsets of quantum efficiencies. Right: The mean charge of the individual DOM SPE templates.

329 The subset of NQE DOMs with the old AC coupling transformer was found to have a 6.1%
 330 narrower Gaussian width and an 8.0% larger Gaussian amplitude (σ and N in Eq. 1.1). The ex-
 331ponential component Exp_2 was also found to have a 7.5% lower E_2 component and a 3.0% higher
 332 $E_{2,\text{component}}$. Although the old toroid DOMs were deployed into the ice earlier than the new
 333 toroid DOMs, the difference above is still noted when examining individual deployment years;
 334 therefore, the shape differences are not attributed to the change in the DOM behavior over time.
 335 However, the DOMs with the old toroids used the first PMTs to be manufactured by Hamamatsu,
 336 so this difference may also be attributed to a gradual change in the process parameters over the
 337 course of PMT manufacturing, i.e., a change in the production procedure rather than the actual AC
 338 coupling version.

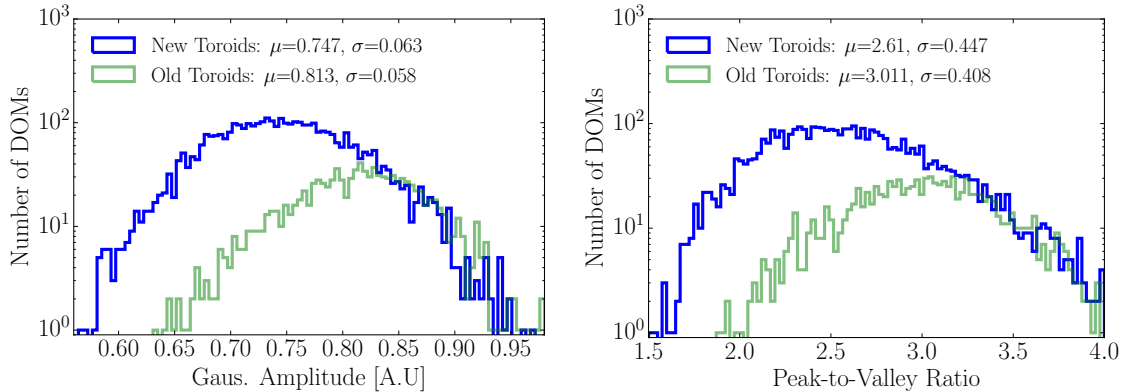


Figure 8. Comparison between the AC coupling versions used on the NQE DOMs. Left: The distribution of the measured Gaussian amplitudes. Right: The distribution of the measured peak-to-valley ratios.

339 **3.2 Quantifying observable changes when modifying the PMT charge distributions**

340 Changing the assumed gain response in simulation, as deduced from data, has different implications
 341 depending on the typical illumination level present in different analyses. These differences are
 342 outlined in the following discussion.

343 The PMT response is described by a combination of a "bare" efficiency, η_0 , and a normalized
 344 charge response function, $f(q)$. The bare efficiency represents the fraction of arriving photons that
 345 result in any nonzero charge response, including those well below the discriminator threshold. The
 346 normalization condition is:

$$\int_0^{\text{inf}} f(q) dq = 1. \quad (3.1)$$

347 Generally, $f(q)$ and η_0 have to be adjusted together to maintain agreement with a quantity known
 348 from lab or in-ice measurements, such as the predicted number of pulses above threshold for a dim
 349 source.

350 **Dim source measurements** Where light levels are low enough, subdiscriminator pulses do not
 351 contribute any observed charge because they do not satisfy the trigger threshold, and the probability
 352 of two photons arriving together is negligible. Given some independent way of knowing the number
 353 of arriving photons, a lab or in-ice measurement determines the trigger fraction above threshold
 354 $\eta_{0.25}$ and/or the average charge over threshold $Q_{0.25}$, either of which can be used to constrain the
 355 model as follows:

$$\eta_{0.25} = \eta_0 \int_{0.25q_{pk}}^{\text{inf}} f(q) dq \quad (3.2)$$

$$Q_{0.25} = \eta_0 \int_{0.25q_{pk}}^{\text{inf}} qf(q) dq \quad (3.3)$$

356 Here, the discriminator threshold is assumed to be 0.25 times the peak position q_{pk} . It is also
 357 useful to multiply observed charges by q_{pk} , since we set each PMT gain by such a reference, and
 358 then a measurement constraint would be stated in terms of $Q_{0.25}/q_{pk}$.

359 **Semi-bright source measurements** Once the ATWD window is open, subsequent pulses are not
 360 limited by the discriminator threshold. WaveDeform introduces a software termination condition at
 361 0.1 PE (described at the end of Section 2.1). The average charge of an individual pulse that arrives
 362 within the time window is:

$$Q_{0.10} = \eta_0 \int_{0.10q_{pk}}^{\text{inf}} qf(q) dq \quad (3.4)$$

363 **Bright source measurements** For light levels that are large, the trigger is satisfied regardless
 364 of the response to individual photons, and the total charge per arriving photon therefore includes
 365 contributions below both the discriminator and the WaveDeform thresholds:

$$Q_0 = \eta_0 \int_0^{\text{inf}} qf(q) dq \quad (3.5)$$

366 As such, the total charge is directly proportional to the average charge of the SPE template,
 367 having a strong dependence on the steeply falling exponential.

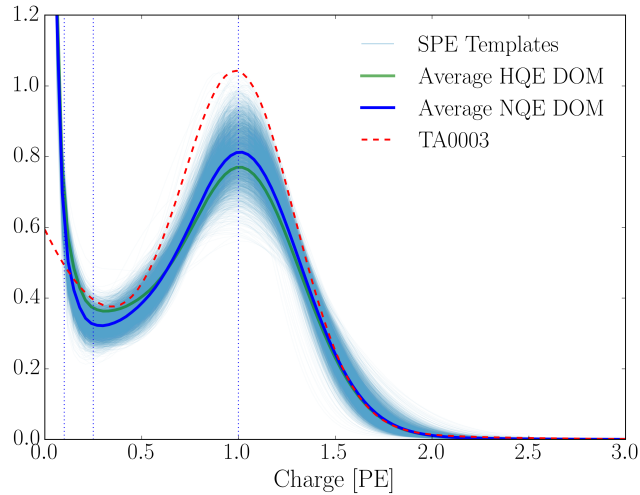


Figure 9. A comparison between the SPE templates (light blue band) and the TA0003 (dashed red line) distribution. The average SPE template for the NQE and HQE DOMs is shown as the thick blue and green lines, respectively. The SPE templates include the residual correction, and all curves are normalized.

3.2.1 Model comparison

When the charge distribution model is changed in a way that preserves agreement with the measured $\eta_{0.25}$ or $Q_{0.25}/q_{pk}$, i.e., η_0 is adjusted properly for changes in $f(q)$, the physical effect can be summarized by the change in the bright-to-dim ratios $Q_0/Q_{0.25}$, and $Q_0/Q_{0.10}$. Conveniently, these ratios depend only on the shape of $f(q)$. Table 3 compares these ratios in terms of the previous charge distribution (TA0003) and the SPE templates described here. It is shown that there are percent level differences in the physically observable bright-to-dim ratios.

Model	Detector	$Q_0/Q_{0.25}$	$Q_0/Q_{0.10}$	$\eta_{0.25}/Q_{0.25}$
TA0003	IceCube and DeepCore	1.017	1.003	0.969
SPE Templates	IceCube	1.031 ± 0.003	1.013 ± 0.001	0.971 ± 0.006
SPE Templates	DeepCore	1.034 ± 0.002	1.014 ± 0.001	0.965 ± 0.006

Table 3. The distribution in bright-to-dim ratios for the previous charge distribution (TA0003) and the individual DOM SPE templates for the IceCube and DeepCore detectors.

Fig. 9 shows the shape difference between the TA0003 distribution and all the SPE templates measured in this report. The shape difference is attributed to better control of the low-charge region, the difference in functional form (described in Section 1.1), and the fact that the SPE templates sample uniformly over the entire photocathode at random incident angles. We have also separated the DOMs into the subsets of NQE and HQE DOMs to illustrate their average shape differences.

3.3 SPE templates in simulation

The IceCube Monte Carlo simulation chain assigns a charge to every photoelectron generated at

382 the surface of the photocathode. The charge is determined by sampling from a normalized charge
 383 distribution probability density function. A comparison between describing the charge distribution
 384 using the SPE templates and the TA0003 distribution follows.

385 Two simulation sets consisting of the same events were processed through the IceCube Monte
 386 Carlo simulation chain to the final level of the multiyear high-energy sterile analysis. At analysis
 387 level, the events that pass the cuts are $>99.9\%$ pure upgoing (directed upwards relative to the
 388 horizon) secondary muons produced by charged current muon neutrino/antineutrino interactions.
 389 The muon energy range of this event selection is between 500 GeV and 10 TeV (reconstructed
 390 quantities).

391 Fig. 10 (left) shows the distribution of the total measured charge in a single DOM during each
 392 event. The data is shown for the full IC86.2012 season but is statistically equivalent to any of the
 393 other seasons. The simulation set using the TA0003 charge distribution is shown in orange, and that
 394 using the SPE templates is shown in blue. The bottom of the plot shows the ratio of the measured
 395 quantity relative to data. Fig. 10 (right) shows the distribution of the measured total charge on a
 396 DOM (after noise removal) divided by the number of channels, or DOMs, that participated in the
 397 event. Both plots in Fig. 10 have been normalized such that the area under the histograms is the
 398 same.

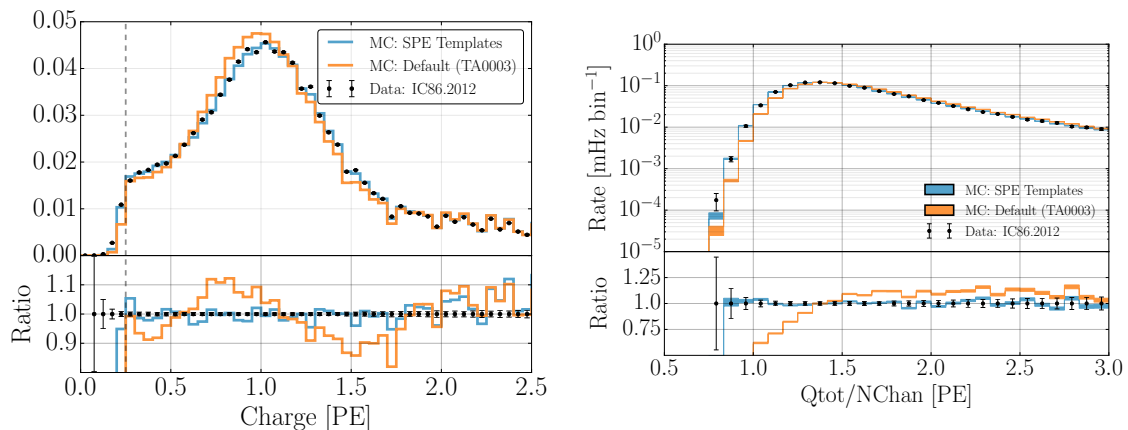


Figure 10. A comparison between the SPE templates (blue) and the TA0003 (orange) model for describing the SPE charge distribution in Monte Carlo. The simulation is compared to the 2012 IceCube season. Left: The total measured charge per DOM, per event at analysis level. Right: The distribution of the total measured charge of an event divided by the number of DOMs that participated in the event.

399 The SPE templates clearly improve the overall MC description of these two variables. IceCube
 400 includes a systematic uncertainty in all analyses, which scales the DOM efficiency to account for
 401 effects that change the total observed charge. This systematic compensates for the overall mean
 402 charge shift introduced using the SPE templates; however, the SPE templates now introduce DOM-
 403 to-DOM differences. This is not expected to change the IceCube physics results since analyses are
 404 sensitive to the overall detector performance rather than the individual DOM variations.

405 3.4 SPE templates for calibration

406 The gain setting on each DOM is calibrated at the beginning of the season such that the Gaussian

407 mean charge distribution corresponds to a gain of 10^7 (equivalently labelled as 1 PE). Since the
408 method used to extract the Gaussian mean described in this report is different from the previous
409 method used for calibration of the DOMs, the total measured charge from a DOM is expected to
410 change with the updated calibration.

411 As shown in Tables 1 and 2, the Gaussian mean component of the fit of every year is found to
412 be on average 2.2% higher than unity, corresponding to a systematic overestimation of the measured
413 charge in the detector. This correction to the measured charge can be implemented retroactively by
414 dividing the reported charge from WaveDeform by the corresponding Gaussian mean for a given
415 DOM. Alternatively, the MC can account for this difference by simply inserting the SPE templates
416 with Gaussian mean matching the values found in the data. Both of these solutions will be used in
417 future IceCube data/MC production.

418 **4. Conclusion**

419 This report outlines the procedure used for collecting a relatively pure sample of single-photoelectron
420 charges for each of the in-ice DOMs in IceCube. MPE contamination was removed under the as-
421 sumption that it is the convolution of the SPE distribution from multiple times.

422 The SPE templates were extracted for each DOM and each season in the IceCube and Deep-
423 Core detectors and investigated for correlations with hardware-related features. Neither detector
424 shows more than a 0.5% deviation in any of the fitted parameters over the investigated seasons, in
425 agreement with Ref. [8]. Yearly variations in the fit parameters are consistent with statistical fluc-
426 tuations. The HQE DOMs located in the IceCube and DeepCore detectors were found to have an
427 Exp_2 component distinguishable from the standard DOMs. Similarly, DOMs with the old method
428 of AC coupling were found to have a narrower and larger Gaussian component. This was not found
429 to be due to a manufacturing process and is still under investigation.

430 The SPE templates were introduced into the MC simulation production and the result was
431 compared to the default charge distribution. A significant improvement in the description of the
432 low-level variables, total charge per DOM, and total charge per event over the number of channels
433 was shown. IceCube includes a systematic that scales the bare efficiency of the DOMs to maintain
434 agreement with a quantity known from lab or in-ice measurements. After accounting for this shift,
435 the effect on physics analysis, as shown by the bright-to-dim ratios, is expected to be minimal
436 (percent level changes in the measured charge).

437 The new method for extracting the calibration constant that determines the gain setting on each
438 of the PMTs (the Gaussian mean of the fit) has been revised and shows that the average gain was
439 approximately $2.2\% \pm 3.1\%$ higher than expected. This will be implemented in future IceCube data
440 reprocessing.

442 **Acknowledgments**

443 We acknowledge the support from the following agencies: U.S. National Science Foundation - Of-
444 fice of Polar Programs, U.S. National Science Foundation - Physics Division, University of Wiscon-
445 sin Alumni Research Foundation, the Grid Laboratory Of Wisconsin (GLOW) grid infrastructure

446 at the University of Wisconsin - Madison, the Open Science Grid (OSG) grid infrastructure; U.S.
447 Department of Energy, and National Energy Research Scientific Computing Center, the Louisiana
448 Optical Network Initiative (LONI) grid computing resources; Natural Sciences and Engineering
449 Research Council of Canada, WestGrid and Compute/Calcul Canada; Swedish Research Council,
450 Swedish Polar Research Secretariat, Swedish National Infrastructure for Computing (SNIC),
451 and Knut and Alice Wallenberg Foundation, Sweden; German Ministry for Education and Re-
452 search (BMBF), Deutsche Forschungsgemeinschaft (DFG), Helmholtz Alliance for Astroparticle
453 Physics (HAP), Research Department of Plasmas with Complex Interactions (Bochum), Germany;
454 Fund for Scientific Research (FNRS-FWO), FWO Odysseus programme, Flanders Institute to en-
455 courage scientific and technological research in industry (IWT), Belgian Federal Science Policy
456 Office (Belspo); University of Oxford, United Kingdom; Marsden Fund, New Zealand; Australian
457 Research Council; Japan Society for Promotion of Science (JSPS); the Swiss National Science
458 Foundation (SNSF), Switzerland; National Research Foundation of Korea (NRF); Villum Fonden,
459 Danish National Research Foundation (DNRF), Denmark.

460 **References**

- 461 [1] J. Ahrens *et al.*, “Icecube preliminary design document,” URL: <http://www.icecube.wisc.edu/science/publications/pdd>, 2001.
- 462
- 463 [2] A. Achterberg, M. Ackermann, J. Adams, J. Ahrens, K. Andeen, D. Atlee, J. Baccus, J. Bahcall,
464 X. Bai, B. Baret, *et al.*, “First year performance of the icecube neutrino telescope,” *Astroparticle*
465 *Physics*, vol. 26, no. 3, pp. 155–173, 2006.
- 466 [3] I. Collaboration *et al.*, “Evidence for high-energy extraterrestrial neutrinos at the icecube detector,”
467 *Science*, vol. 342, no. 6161, p. 1242856, 2013.
- 468 [4] R. Abbasi, Y. Abdou, T. Abu-Zayyad, M. Ackermann, J. Adams, J. Aguilar, M. Ahlers, M. Allen,
469 D. Altmann, K. Andeen, *et al.*, “The design and performance of icecube deepcore,” *Astroparticle*
470 *physics*, vol. 35, no. 10, pp. 615–624, 2012.
- 471 [5] R. Abbasi, M. Ackermann, J. Adams, M. Ahlers, J. Ahrens, K. Andeen, J. Auffenberg, X. Bai,
472 M. Baker, S. Barwick, *et al.*, “The icecube data acquisition system: Signal capture, digitization, and
473 timestamping,” *Nuclear Instruments and Methods in Physics Research Section A: Accelerators,*
474 *Spectrometers, Detectors and Associated Equipment*, vol. 601, no. 3, pp. 294–316, 2009.
- 475 [6] Hamamatsu, “Datasheet,” URL: <https://www.hamamatsu.com/>, 2018.
- 476 [7] R. Abbasi, Y. Abdou, T. Abu-Zayyad, J. Adams, J. Aguilar, M. Ahlers, K. Andeen, J. Auffenberg,
477 X. Bai, M. Baker, *et al.*, “Calibration and characterization of the icecube photomultiplier tube,”
478 *Nuclear Instruments and Methods in Physics Research Section A: Accelerators, Spectrometers,*
479 *Detectors and Associated Equipment*, vol. 618, no. 1-3, pp. 139–152, 2010.
- 480 [8] M. Aartsen *et al.*, “The icecube neutrino observatory: Instrumentation and online systems, jinst 12
481 (03)(2017) p03012,” *arXiv preprint arXiv:1612.05093*, pp. 1748–0221.
- 482 [9] R. Stokstad, “Design and performance of the icecube electronics,” 2005.
- 483 [10] Hamamatsu, “Resources: Basics and applications,” URL:
484 https://www.hamamatsu.com/resources/pdf/etd/PMT_handbook_v3aE.pdf, 2018.
- 485 [11] Hamamatsu, “Handbook resources, chapter 4,” URL:
486 https://www.hamamatsu.com/resources/pdf/etd/PMT_handbook_v3aE-Chapter4.pdf, 2018.
- 487 [12] J. Brack, B. Delgado, J. Dhooghe, J. Felde, B. Gookin, S. Grullon, J. Klein, R. Knapik, A. LaTorre,
488 S. Seibert, *et al.*, “Characterization of the hamamatsu r11780 12 in. photomultiplier tube,” *Nuclear*
489 *Instruments and Methods in Physics Research Section A: Accelerators, Spectrometers, Detectors and*
490 *Associated Equipment*, vol. 712, pp. 162–173, 2013.
- 491 [13] E. Calvo, M. Cerrada, C. Fernández-Bedoya, I. Gil-Botella, C. Palomares, I. Rodríguez, F. Toral, and
492 A. Verdugo, “Characterization of large-area photomultipliers under low magnetic fields: Design and
493 performance of the magnetic shielding for the double chooz neutrino experiment,” *Nuclear*
494 *Instruments and Methods in Physics Research Section A: Accelerators, Spectrometers, Detectors and*
495 *Associated Equipment*, vol. 621, no. 1-3, pp. 222–230, 2010.
- 496 [14] F. Kaether and C. Langbrandtner, “Transit time and charge correlations of single photoelectron events
497 in r7081 photomultiplier tubes,” *Journal of Instrumentation*, vol. 7, no. 09, p. P09002, 2012.
- 498 [15] B. Lubsandorzhev, P. Pokhil, R. Vasiljev, and A. Wright, “Studies of prepulses and late pulses in the
499 8" electron tubes series of photomultipliers,” *Nuclear Instruments and Methods in Physics Research*
500 *Section A: Accelerators, Spectrometers, Detectors and Associated Equipment*, vol. 442, no. 1-3,
501 pp. 452–458, 2000.

- 502 [16] K. Ma, W. Kang, J. Ahn, S. Choi, Y. Choi, M. Hwang, J. Jang, E. Jeon, K. Joo, H. Kim, *et al.*, “Time
503 and amplitude of afterpulse measured with a large size photomultiplier tube,” *Nuclear Instruments
504 and Methods in Physics Research Section A: Accelerators, Spectrometers, Detectors and Associated
505 Equipment*, vol. 629, no. 1, pp. 93–100, 2011.
- 506 [17] S. Torre, T. Antonioli, and P. Benetti, “Study of afterpulse effects in photomultipliers,” *Review of
507 scientific instruments*, vol. 54, no. 12, pp. 1777–1780, 1983.
- 508 [18] M. Aartsen, K. Abraham, M. Ackermann, J. Adams, J. Aguilar, M. Ahlers, M. Ahrens, D. Altmann,
509 T. Anderson, M. Archinger, *et al.*, “Characterization of the atmospheric muon flux in icecube,”
510 *Astroparticle physics*, vol. 78, pp. 1–27, 2016.
- 511 [19] M. Aartsen, R. Abbasi, Y. Abdou, M. Ackermann, J. Adams, J. Aguilar, M. Ahlers, D. Altmann,
512 J. Auffenberg, X. Bai, *et al.*, “Measurement of south pole ice transparency with the icecube led
513 calibration system,” *Nuclear Instruments and Methods in Physics Research Section A: Accelerators,
514 Spectrometers, Detectors and Associated Equipment*, vol. 711, pp. 73–89, 2013.
- 515 [20] M. Aartsen, R. Abbasi, M. Ackermann, J. Adams, J. Aguilar, M. Ahlers, D. Altmann, C. Arguelles,
516 J. Auffenberg, X. Bai, *et al.*, “Energy reconstruction methods in the icecube neutrino telescope,”
517 *Journal of Instrumentation*, vol. 9, no. 03, p. P03009, 2014.
- 518 [21] R. Dossi, A. Ianni, G. Ranucci, and O. J. Smirnov, “Methods for precise photoelectron counting with
519 photomultipliers,” *Nuclear Instruments and Methods in Physics Research Section A: Accelerators,
520 Spectrometers, Detectors and Associated Equipment*, vol. 451, no. 3, pp. 623–637, 2000.